applied sciences

MDPI

Article

Exceptional Points in Non-Hermitian Photonic Crystals Incorporated With a Defect

Fangmei Liu [1,†], Dong Zhao [1], Hui Cao [2,†], Bin Xu [3,*], Wuxiong Xu [1,*] and Shaolin Ke [4]

1 Laboratory of Functional Materials and Devices for Informatics, Hubei University of Science and Technology, Xianning 437100, China; liufangmei@hbust.edu.cn (F.L.); zhaodong@hbust.edu.cn (D.Z.)
2 School of Mathematics and Statistics, Hubei University of Science and Technology, Xianning 437100, China; caohui@hbust.edu.cn
3 School of Computer Science and Technology, Hubei University of Science and Technology, Xianning 437100, China
4 Hubei Key Laboratory of Optical Information and Pattern Recognition, Wuhan Institute of Technology, Wuhan 430205, China; keshaolin@wit.edu.cn
* Correspondence: jwcxb@hbust.edu.cn (B.X.); xwxiong@hbust.edu.cn (W.X.)
† These authors contributed equally to this work.

Received: 20 December 2019; Accepted: 20 January 2020; Published: 23 January 2020

Abstract: We explored exceptional points (EPs) in one dimensional non-Hermitian photonic crystals incorporated with a defect. The defect was asymmetric with respect to the center. Two EPs could be derived by modulating the normalized frequency and the gain-loss coefficient of defect. The reflection coefficient complex phase changed dramatically around EPs, and the change in complex phase was π at EPs. The electric field of EPs was mainly restricted to the defect, which can induce a giant Goos–Hänchen (GH) shift. Moreover, we found a coherent perfect absorption-laser point (CPA-LP) in the structure. A giant GH shift also existed around the CPA-LP. The study may have found applications in highly sensitive sensors.

Keywords: exceptional point; non-Hermite; photonic crystal; defect; Goos–Hänchen shift

1. Introduction

Non-Hermite, which stems from quantum mechanics [1], has promptly expanded to optics [2–5], acoustics [6], and electronics [7]. Systems including gain or loss are non-Hermitian [8–12]. There is an energy exchange between non-Hermitian systems and the external environment. Compared with the quantum structures, gain and loss in optics are relatively easy to realize [13–15], so non-Hermitian optics has become an intriguing research subject. The eigenvalues of Hamiltonian are real in Hermitian systems, while they are generally complex in non-Hermitian systems. However, as the Hamiltonian in optical systems meets parity-time (PT) symmetry, that is, the refractive indices of materials are satisfying $n(\boldsymbol{r}) = n^*(-\boldsymbol{r})$ [16,17], the eigenvalues can be real. The PT-symmetry will spontaneously break if the gain and loss surpass some critical value, which is defined as the exceptional point (EP) [8,13]. The eigenvalues and eigenvectors of Hamiltonian degenerate in non-Hermitian systems at the EPs, around which many fascinating optical properties may be induced, consist of sharp changes in the complex phase [18], unidirectional invisibility [19,20], and topological boundary states [21].

In recent years, complex photonic crystals (PCs) have provided a new opportunity to explore the non-Hermitian optical properties and other nonlinearities theoretically and experimentally [22–28]. Many significant optical characteristics have been discovered in PCs, such as solitons [29–33], topological modes [34,35], and strong absorptions [36–39]. Furthermore, there are bandgap structures in the transmission spectra as light impinges upon PCs, and light field localization can also be implemented

in defective PCs, which could be utilized for enhancing the nonlinearity of materials [40,41] and the lateral shifts of reflected beams [42–45].

EPs and coherent perfect absorption-laser points (CPA-LPs) exist in PT-symmetric PCs [46]; however, it is more difficult to make complex dielectrics obey PT symmetry experimentally. Here, we embedded a defect in PCs. The refractive index of the defect is complex and the imaginary part of the refractive index (denoted by a gain-loss coefficient σ) can be tuned. We searched EPs and CPA-LPs in the parameter space composed of the frequency and gain-loss coefficient. We then explored the complex phase changes of reflection and transmission coefficients around EPs and CPA-LPs. Next, we investigated the degeneration of the eigenvalues of Hamiltonian at EPs and gave the distribution of the electric field. Finally, we simulated the Goos–Hänchen (GH) shift of reflected and transmitted beams around EPs and CPA-LPs.

2. Non-Hermitian Photonic Crystals

We constructed the non-Hermitian PCs, which were composed of two Bragg gratings and a defect, as shown in Figure 1. Two different dielectrics, A and B, arrayed alternatively to form two Bragg gratings. The dielectrics A and B were MgF_2 and ZnS, respectively. The defect containing dielectrics C and D was embedded in the Bragg gratings. The dielectrics C and D could be obtained by doping SiO_2 with high and low impurities of refractive indices, respectively. We denoted the refractive indices of dielectrics by n_a, n_b, n_c, and n_d, respectively. The thickness of each layer was set as a quarter of the optical wavelength, *viz*, $L_{a,b,c,d} = \lambda_0/4n_{a,b,c,d}$, where $\lambda_0 = 100$ μm is the midgap wavelength of the defect PCs. The refractive indices of materials were $n_a = 1.38$, $n_b = 2.35$, $n_c = 1.4 + 0.01\sigma i$, and $n_d = 1.6 + 0.01\sigma i$, respectively, where σ is the gain-loss coefficient. The positive gain-loss coefficient represented loss and the negative gain-loss coefficient represented gain. The gain in the defect could be realized by doping Ge/Cr or nonlinear two-wave mixing [47,48], and the loss of material could be achieved by acoustic modulators [49]. The designed PCs could also be abbreviated to $(AB)^N CD(BA)^N$, where N is the periodic number of Bragg gratings, and here it shows $N = 5$.

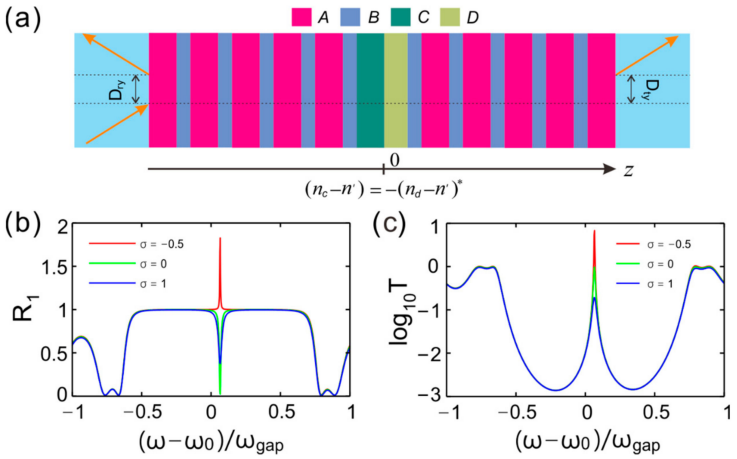

Figure 1. (**a**) Schematic of one-dimensional non-Hermitian photonic crystals. The primitive unit-cell layers, A and B, array alternatively to form two Bragg gratings. The defect composed of dielectrics C and D is asymmetric with respect to the center. D_{ry} and D_{ty} are the lateral Goos–Hänchen shifts of the reflected beam and transmitted beam, respectively. (**b**,**c**) Reflectance and transmittance spectra for three specific values of the gain-loss coefficient, respectively. The asterisk represents complex conjugate operations.

In simulations, the incident wavelength was in the range of terahertz band and the transmission matrix method (TMM) was used to derive the reflection coefficient r and transmission coefficient t [18]. Subsequently, the reflectance of light and transmittance can be denoted by $R = rr^*$ and $T = tt^*$, respectively. The reflection coefficient is generally complex and can be expressed as $r/t = |r/t|\exp(i\varphi_{r/t})$,

where $\varphi_{r/t}$ is the complex phase of the reflection/transmission coefficient. As a transverse magnetic (TM) polarization wave obliquely impinged upon the PC with the incident angle θ, the lateral GH shift of reflected/transmitted light beam was proportional to the slope of the reflection/transmission coefficient complex phase, with respect to the incident angle, that is $D_{ry/ty} = -\lambda d\varphi_{r/t}/2\pi d\theta$ [18], where λ is the incident wavelength.

We set the incident light as a TM wave, and the incident angle was $\theta = 20°$. When light obliquely impinged upon the PCs from the left, Figure 2a provides the reflectance spectra for three different values of gain-loss coefficient σ, where $(\omega - \omega_0)/\omega_{gap}$ is the normalized frequency and $\omega_{gap} = 4\omega_0 \arcsin|(n_b - n_a)/(n_b + n_a)|^2/\pi$ is the photonic bandgap [50]. The center frequency of the bandgap was defined as $\omega_0 = 2\pi c/\lambda_0$. One can see that there was a bandgap structure in the reflectance spectrum for each fixed coefficient and a defect mode located at the middle of the bandgap. The reflectance of defect mode was zero, *viz.* $R_1 = 0$ was the coefficient $\sigma = 0$. For $\sigma > 0$, such as $\sigma = 1$, the reflectance $1 > R_1 > 0$ and a partial incident light was reflected by the PCs. The reflectance surpassed 1 as the coefficient $\sigma < 0$. The loss and gain in the defect can both enhance the reflectance of the defect mode. Figure 2b gives the transmittance varying with the normalized frequency. Light could not transmit the PCs as the frequency of wave was in the range of the bandgap, except for the defect mode. As $\sigma = 1$, the incident wave could overall pass through the structure for the defect mode, i.e., $T = 1$. The transmittance was $T < 1$ for the defect mode as the coefficient was $\sigma > 1$, while the transmittance was $T > 1$ for the defect mode as the coefficient was $\sigma < 1$. The loss or gain in the defect can reduce or enhance the reflectance of the defect mode, respectively.

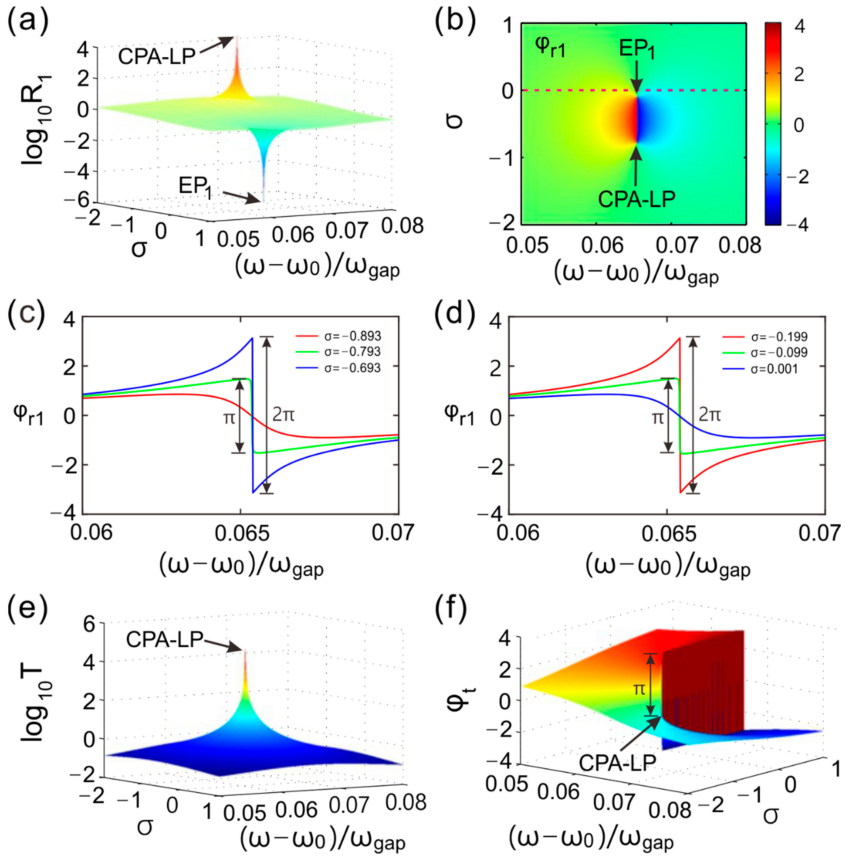

Figure 2. (**a**,**b**) Reflectance and complex phase of reflection coefficient, respectively. (**c**,**d**) Complex phase of reflection coefficient varying with the normalized frequency around the coherent perfect absorption-laser point (CPA-LP) and exceptional point $(EP)_1$. (**e**,**f**) Transmittance and complex phase of transmission coefficient. The parameter space is composed of the normalized frequency and gain-loss coefficient. Light is incident from the left.

3. Exceptional Points and Sharp Change in Phase

Figure 2a demonstrates the reflectivity in the parameter space composed of the normalized frequency $(\omega - \omega_0)/\omega_{gap}$ and gain-loss coefficient. One can see there is a peak and a valley in the parameter space. The peak value was $R_1 = 1.03 \times 10^5$ and it can be viewed as $+\infty$ in our calculating accuracy. The maximum point was the CPA-LP, which located at $[(\omega_{LP} - \omega_0)/\omega_{gap} = 0.0654, \sigma_{LP} = -0.79]$. The valley located at $[(\omega_{EP1} - \omega_0)/\omega_{gap} = 0.0654, \sigma_{EP1} = -0.1]$ and was an EP labeled by EP_1. The reflectance of light at EP_1 was $R_1 = 1.33 \times 10^{-6}$, which is approximately equal to 0 in our calculating accuracy. The non-Hermitian system can be viewed as a resonant cavity, of which the defect is the cavity body and the Bragg gratings are reflectors. The resonance cavity and gain-loss coefficient of the defect collectively induced the CPA-LP and EP_1. Next, we demonstrate the characteristics which approve the CPA-LP and EP.

For the light incident from the left, the reflection coefficient can be written as $r_1 = |r_1|\exp(i\varphi_{r1})$, where φ_{r1} is the complex phase of reflection coefficient, as shown in Figure 2b. The EP_1 and CPA-LP were two singular points in the complex phase of the reflection coefficient. The complex phase φ_{r1} sharply changes around the EP_1 and CPA-LP. That is, a slight increase in the normalized frequency or in the gain-loss coefficient may lead to a great variation in the complex phase near the EP_1 and CPA-LP. For three specific values $\sigma = -0.893, -0.793$, and -0.693, which were near the CPA-LP, Figure 2c provides the complex phase of reflection coefficient varying with the normalized frequency. For the coefficient $\sigma = -0.793$, approaching to σ_{LP}, the complex phase change was $\pm\pi$ around the CPA-LP as the frequency increased. For $\sigma = -0.893$, lower than σ_{LP}, the slope of complex phase curve was negative, while for $\sigma = -0.693$, larger than σ_{LP}, the slope of complex phase curve was positive and there was a meaningless 2π hopping in the complex phase. Figure 2d demonstrates the complex phase cures for three given values, $\sigma = -0.199, -0.099$, and 0.001, around the EP_1. One can see that the complex phase change was also $\pm\pi$ as the coefficient approached σ_{EP1}, such as $\sigma = -0.099$. Different from the situation near the CPA-LP, the slope of complex phase curve was positive as the coefficient $\sigma < \sigma_{EP1}$, while the slope was negative as $\sigma > \sigma_{EP1}$ around the EP_1. The common characteristic was that the closer the parameters were to the CPA-LP and EP_1, the higher the slope of curve was, which may have resulted in a giant GH shift.

Figure 2e shows the transmittance light in the parameter space. There was a peak in transmission in the parameter space as the normalized frequency and gain-loss coefficient changed. The maximum point was exactly at the CPA-LP, which approves the properties of the CPA laser state. The maximum transmittance was $T_{LP} = 1.34 \times 10^5$, which can be viewed as $+\infty$ in our accuracy. The CPA-LP is a boundary state (the power of mode is mainly restricted at the interface of two different materials). The complex phase of transmission coefficient changed dramatically with the parameters around the CPA-LP, as shown in Figure 2f. There was a hopping in the complex phase of transmission coefficient at the CPA-LP and the variation was $\pm\pi$. The hopping was meaningless $\pm2\pi$ at the other complex phase jump points, where the complex phase could therefore be viewed to be continuous. The resonance of defect cavity and the gain in dielectrics acted together to result in the CPA-LP. The extreme value in transmittance meant that there was complex phase uncertainty of the transmission coefficient. The sharp change in the complex phase of the transmission coefficient can also induce the lateral GH shift of the transmitted light.

As the light incident from the right, the reflection coefficient was denoted by $r_2 = |r_2|\exp(i\varphi_{r2})$. Figure 3a gives the reflectance in the parameter space. There were also two extreme points as the normalized frequency and gain-loss coefficient increased. The minimum was labeled by EP_2 and located at $[(\omega_{EP1} - \omega_0)/\omega_{gap} = 0.0654, \sigma_{EP2} = 0.1]$, while the maximum was the CPA-LP and located at $[(\omega_{LP} - \omega_0)/\omega_{gap} = 0.0654, \sigma_{LP} = -0.79]$. The positive gain-loss coefficient represented loss and negative gain-loss coefficient represented gain, respectively. When light was incident from the left, the position of EP_1 showed that gain in materials was required, and while the light was incident from the right, loss was required to carry out the singularity of EP_2. These properties indicate that the

EPs were dependent on the directions of light incident form the left and right. The dependence on directions for EPs resulted from the asymmetry of the defect and the non-Hermiticity of PCs.

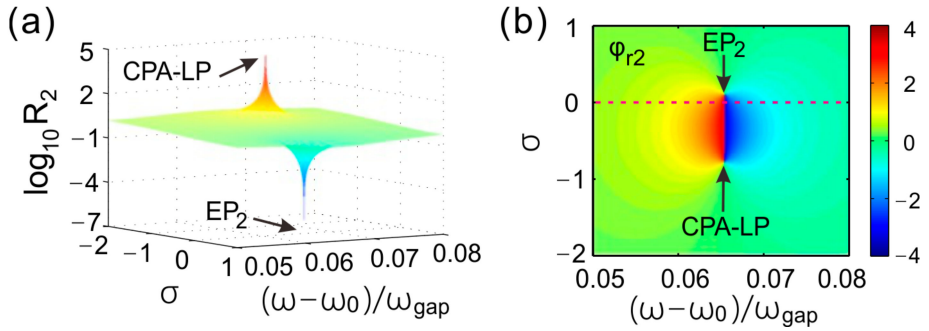

Figure 3. (**a**,**b**) Reflectance and complex phase of reflection coefficient varying with normalized frequency and gain-loss coefficient for a light incident from the right, respectively.

As the gain-loss coefficient σ changed, the real and imaginary parts of eigenvalues are depicted in Figure 4a,b, respectively. For the incident and scattered waves, the scattering matrix in PCs can be written as $S = [t\ r_1; r_2\ t]$, which is the counterpart of Hamiltonian in quantum systems [51,52]. The eigenvalues of *S*-matrix were $\lambda_{1,2} = t \pm (r_1 r_2)^{1/2}$ and the eigenvectors were $(r_1{}^{1/2}, \pm r_2{}^{1/2})$. The eigenvalues coalesce and the eigenvectors degenerated at $(r_1 r_2)^{1/2} = 0$, which was defined as EPs of eigenvalues. That is, the EPs could be derived by r_1 or $r_2 = 0$. We generally searched for EPs in the parameter space on conditions of R_1 or $R_2 = 0$. The reflection coefficient complex phase φ_{r1} and φ_{r2} were bound to experience a dislocation as $R_1 R_2 = 0$, which is an unique characteristic of EPs. The zero reflection and complex phase dislocation can be utilized to seek out EPs. When $\sigma < \sigma_{EP1}$ and $\sigma > \sigma_{EP2}$, the real parts of the eigenvalues split into two branches. When $\sigma_{EP1} < \sigma < \sigma_{EP2}$, the real parts of eigenvalues degenerated. On the whole, the curves of real parts were anti-crossing and the imaginary part curves were crossing around the EPs for the eigenvalues. The imaginary parts of eigenvalues degenerated at EPs as well. These characteristics are often used to confirm EPs.

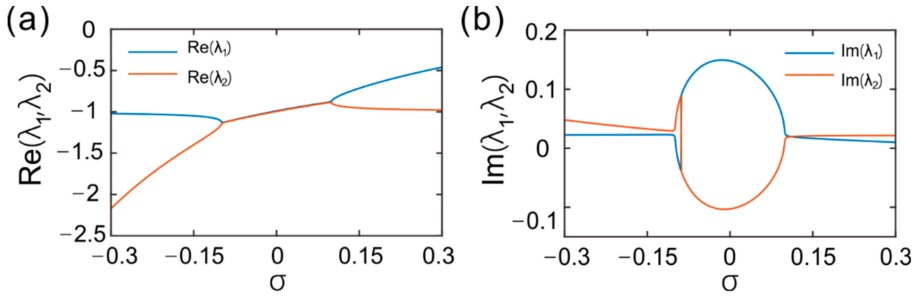

Figure 4. (**a**,**b**) Real and imaginary parts of Hamiltonian eigenvalues varying with the gain-loss coefficient around the EPs, respectively.

4. Applications and Giant GH Shift

Figure 5a gives the distribution of the electric field for EP_1. It demonstrates that the power of electric field was mainly restrained in the defect. The electric field intensity decreased exponentially as the coordinate extended to the left and right from the 0 point. The distribution of electric field further manifested that EP_1 was the defect state (or transmission state). Figure 5b provides the electric field distribution of CPA-LP. The electric field mainly distributed the defect as well. This means that CPA-LP was also a defect state. Two Bragg gratings formed the resonance of cavity, together with some appropriate gain in defect, to result in the CPA laser state.

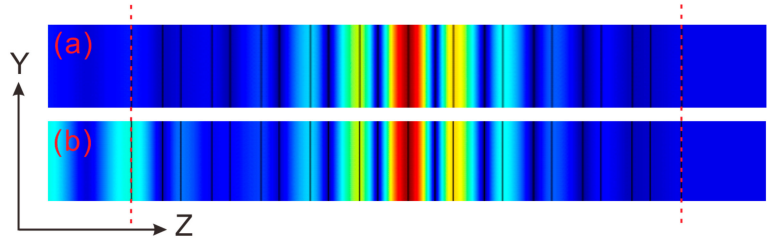

Figure 5. (**a**) Electric field distribution of EP_1. (**b**) Electric field distribution of CPA-LP.

In the parameter space, the complex phase of the reflection coefficient changed sharply as the normalized frequency and gain-loss coefficient increased near EPs and CPA-LP. Figure 6a gives the GH shift of reflected light around EP_1 and CPA-LP. The interested area is divided into three parts by dotted lines. EP_1 and CPA-LP are exactly on the dotted lines. At EP_1 and CPA-LP, one can see that the GH shift was infinite, so EP_1 and CPA-LP were the singularity of the GH shift. Except for EP_1 and CPA-LP, the GH shift on the dotted lines was 0. Otherwise, the GH shift in region I and III was positive, while the GH shift in region II was negative. The GH shift was greater as the parameters increasingly approached EP_1 and CPA-LP. In our accuracy, the positive GH shift could be as high as $10^6\lambda$, and the negative GH shift could be as high as $-10^5\lambda$. The sharp change in the complex phase of reflection coefficient near EPs and CPA-LP generated the giant GH shift. The singularity of the GH shift at EPs and CPA-LP was also an intriguing characteristic.

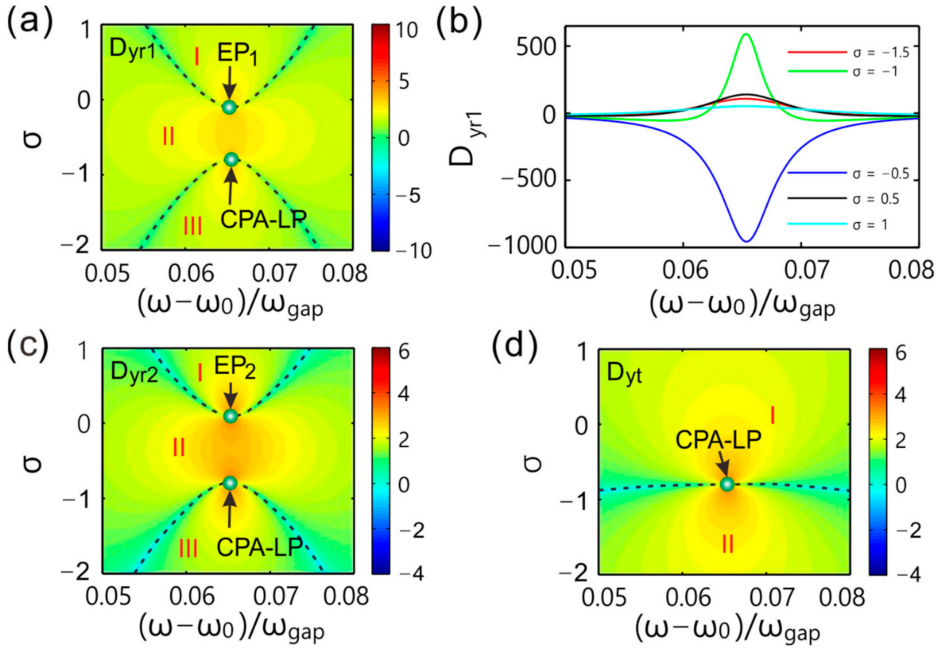

Figure 6. (**a**,**c**) Lateral Goos–Hänchen (GH) shift of reflected light beam from the left and right, respectively. (**b**) GH shift for three special gain-loss coefficients versus normalized frequency. (**d**) Lateral GH shift of transmitted light beam. The parameter space is composed of the normalized frequency and gain-loss coefficient. It has rescaled the GH shift by taking logarithm $\log_{10}|D_y|$ for clarity for (**a**,**c**,**d**).

Figure 6b illustrates the relationship between the GH shift and normalized frequency for five special gain-loss coefficients $\sigma = -1.5, \pm 1$ and ± 0.5. One can see that the GH shift changed with the normalized frequency. There was a peak in each curve as the coefficient $\sigma > \sigma_{EP1}$ or $\sigma < \sigma_{LP}$ and a valley existed in each curve as $\sigma_{LP} < \sigma < \sigma_{EP1}$. The positive and negative maximum GH shifts were at the normalized frequency $(\omega - \omega_0)/\omega_{gap} = 0.0654$. The incident beam was composed of many different frequency components of plane waves. We have showed that the light field penetrated more deeply

into the PCs as the parameters became closer to EP_1 and CPA-LP, so the dispersion of plane waves was more serious. For this reason, the reflected beam consisting of scattering waves had a giant lateral shift.

Figure 6c gives the GH shift around EP_2 and CPA-LP as light was incident from the right. Similarly, EP_2 and CPA-LP were the singular points of the GH shift. Along the dotted lines, the GH shift was 0. The GH shift in region I and III was positive, while the shift in region II was negative. The maximum positive and negative GH shifts were $10^5\lambda$ and $-10^4\lambda$, respectively, indicating that the GH shift of the reflected light from the right was smaller than that of the reflected light from the left. Therefore, the GH shift of the reflected beam was dependent on the direction incident from the left and right.

The lateral shift also existed in the transmitted light. Figure 6d shows the GH shift of the transmitted light beam near CPA-LP. The region was divided into two parts by the dotted line. The GH shift in part I was positive, while the GH shift in part II was negative. The positive and negative GH shifts were $2 \times 10^4\lambda$ and $-6.5 \times 10^4\lambda$, respectively. CPA-LP was the singular point for the GH shift and the GH shift was infinite at CPA-LP. The GH shift along the dotted line was 0. Even though the CPA laser state was not stable enough, the incident light and transmitted light were located at the two sides of the PCs, respectively. Therefore, the spatial discrimination of sensors based on the GH shift of the transmitted beam was better than that of sensors based on the GH shift of the reflected beam.

Based on the GH shift, the PCs can be utilized for highly sensitive sensors in probing the gain or loss factor of materials. Here, we take the normalized frequency $(\omega - \omega_0)/\omega_{gap} = 0.065$, for example, to demonstrate the application. To make the phenomenon more obvious, the given normalized frequency was near ω_{LP} and ω_{EP}. Figure 7a shows the lateral GH shift. One can see that the GH shift changed with the gain-loss coefficient of the defect and there were positive and negative GH shifts around the EPs and LP. The positive and negative maxima could reach as high as the magnitude of $10^3\lambda$. Figure 7b gives the sensitivity coefficient of sensors based on the GH shift in defecting gain or loss coefficient of materials. The maximum sensitivity coefficient (SC) was 6.65×10^4, since the frequency of incident wave was fixed. The SC can be further improved if the chosen frequency is closer to ω_{LP} and ω_{EP}. Different from our one-dimensional PC of the multilayer type, PC fibers can also utilized for highly sensitive sensors for temperature sensing application via a Sagnac interferometer [53] or for detection of high refractive index liquid analytes via surface plasmon resonance [54].

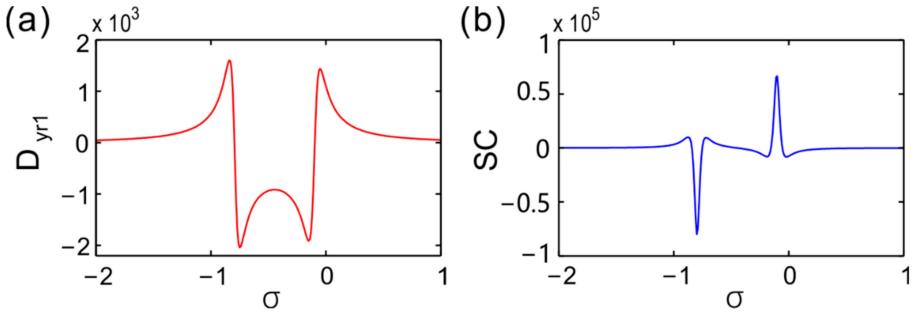

Figure 7. (**a**) Lateral GH shift varying with the gain-loss coefficient. (**b**) Sensitivity coefficient (SC) of sensors used for detecting the gain-loss coefficient of material based on the GH shift. The normalized frequency is $(\omega - \omega_0)/\omega_{gap} = 0.065$ for (**a**,**b**).

The incident angle was selected as 20° and the purpose was to take a specific incident angle as an example to demonstrate that EPs and CPA-LP can be induced in the parameter space when a TM wave is obliquely incident into the non-Hermitian PCs. EPs and the CPA-LP can also be derived as the incident angle is chosen as some other values. The positions of EPs and the CPA-LP changed with the incident angle in the parameter space. If the incident wave was transverse electromagnetic (TE) wave instead, EPs and CPA-LP could also obtained, while the lateral shift of the reflected beam was defined as the Imbert–Federov shift in this case [55].

5. Conclusions

To summarize, we have theoretically studied EPs in one-dimensional non-Hermitian PCs incorporated with a defect. The defect which contains gain and loss is asymmetric with respect to the center. Two EPs have been searched by increasing the normalized frequency and gain-loss coefficient of defect. EPs are directionally dependent on the light incident from the left and right. The complex phases of the reflection and transmission coefficients changed dramatically with the parameters around EPs and there was a phase hopping of $\pm\pi$ at EPs. The electric field of EPs mainly distributed at the center and EPs were confirmed to be defect modes. A giant GH shift of reflected and transmitted light beams was induced around EPs. A CPA-LP was also found in the parameter space and a giant GH shift existed around the CPA-LP as well. EPs and the CPA-LP were singularities of the GH shift. This research provides an option for development in highly sensitive sensors.

Author Contributions: Data curation, W.X.; formal analysis, F.L. and W.X.; funding acquisition, F.L., S.K. and W.X.; investigation, D.Z. and H.C.; project administration, W.X.; resources, D.Z.; software, F.L. and D.Z.; supervision, B.X. and S.K.; visualization, D.Z.; writing—original draft, F.L.; writing—review & editing, H.C., B.X. and S.K. All authors have read and agreed to the published version of the manuscript.

Funding: This research was funded by the National Natural Science Foundation of China (51479155, 11804259, 51975542); the Colleges and Universities of National Innovation and Entrepreneurship the Training Plan (S201910927024); the Scientific Research Project of Hubei University of Science and Technology (2018-20XB010, KY14051, BK202017, HKCXTD-001); the Science and Technology Plan Research Project of Hubei Education Department (B2019162); and the Research and Development Project of Xianning Municipal Science and Technology Bureau (XNKJ-28).

Conflicts of Interest: The authors declare no conflict of interest.

References

1. Bender, C.M.; Boettcher, S. Real spectra in non-Hermitian Hamiltonians having PT symmetry. *Phys. Rev. Lett.* **1998**, *80*, 5243–5246. [CrossRef]
2. Xu, S.L.; Petrovi, N.; Belić, M.R.; Deng, W. Exact solutions for the quintic nonlinear Schrödinger equation with time and space. *Nonlinear Dyn.* **2017**, *84*, 251–259. [CrossRef]
3. Xu, S.L.; Petrović, N.; Belić, M.R. Exact solutions of the (2 + 1)-dimensional quintic nonlinear Schrödinger equation with variable coefficients. *Nonlinear Dyn.* **2015**, *80*, 583–589. [CrossRef]
4. Ke, S.; Zhao, D.; Liu, Q.; Wu, S.; Wang, B.; Lu, P. Optical imaginary directional couplers. *J. Lightwave Technol.* **2018**, *36*, 2510–2515. [CrossRef]
5. Wang, H.; Kong, W.; Zhang, P.; Li, Z.; Zhong, D. Coherent perfect absorption laser points in one-dimensional anti-parity–time-symmetric photonic crystals. *Appl. Sci.* **2019**, *9*, 2738. [CrossRef]
6. Zhu, X.; Ramezani, H.; Shi, C.; Zhu, J.; Zhang, X. PT-symmetric acoustics. *Phys. Rev. X* **2014**, *4*, 031042. [CrossRef]
7. Ezawa, M. Electric circuits for non-Hermitian Chern insulators. *Phys. Rev. B* **2019**, *100*, 081401. [CrossRef]
8. Ke, S.; Wang, B.; Qin, C.; Long, H.; Wang, K.; Lu, P. Exceptional points and asymmetric mode switching in plasmonic waveguides. *J. Lightwave Technol.* **2016**, *34*, 5258–5262. [CrossRef]
9. He, J.R.; Xu, S.; Xue, L. Generation of high-power parabolic pulses in quantum dot waveguide amplifiers. *Optik* **2019**, *182*, 1106–1112. [CrossRef]
10. He, J.R.; Xu, S.; Xue, L. Snakelike similaritons in tapered grating dual-core waveguide amplifiers. *Phys. Scr.* **2019**, *94*, 105216. [CrossRef]
11. Ke, S.; Liu, Q.; Zhao, D.; Liu, W. Spectral discrete diffraction with non-Hermitian coupling. *J. Opt. Soc. Am. B* **2018**, *35*, 2387–2393. [CrossRef]
12. Ke, S.; Zhao, D.; Liu, Q.; Liu, W. Adiabatic transfer of surface plasmons in non-Hermitian graphene waveguides. *Opt. Quantum Electron.* **2018**, *50*, 393. [CrossRef]
13. Liu, Q.; Wang, B.; Ke, S.; Long, H.; Wang, K.; Lu, P. Exceptional points in Fano-resonant graphene metamaterials. *Opt. Express* **2017**, *25*, 7203–7212. [CrossRef] [PubMed]
14. Xu, S.L.; Belić, M.R. Three-dimensional Hermite-Bessel solitons in strongly nonlocal media with variable potential coefficients. *Opt. Commun.* **2014**, *313*, 62–69. [CrossRef]

15. Li, Z.; Xu, Z.; Qu, X.; Wang, S.; Peng, J. Pattern transfer of hexagonal packed structure via ultrathin metal nanomesh masks for formation of Si nanopore arrays. *J. Alloys Compd.* **2017**, *695*, 458–461. [CrossRef]
16. Xu, S.L.; Zhao, Y.; Petrović, N.Z.; Belić, M.R. Spatiotemporal soliton supported by parity-time symmetric potential with competing nonlinearities. *EPL* **2016**, *115*, 14006. [CrossRef]
17. Xu, S.L.; Petrović, N.; Belić, M.R.; Hu, Z.L. Light bullet supported by parity-time symmetric potential with power-law nonlinearity. *Nonlinear Dyn.* **2016**, *84*, 1877–1882. [CrossRef]
18. Zhao, D.; Ke, S.; Liu, Q.; Wang, B.; Lu, P. Giant Goos-Hänchen shifts in non-Hermitian dielectric multilayers incorporated with graphene. *Opt. Express* **2018**, *26*, 2817–2828. [CrossRef]
19. Lin, Z.; Ramezani, H.; Eichelkraut, T.; Kottos, T.; Cao, H.; Christodoulides, D.N. Unidirectional invisibility induced by PT-symmetric periodic structures. *Phys. Rev. Lett.* **2011**, *106*, 213901. [CrossRef]
20. Cao, H.; Zhao, D.; Fang, M.; Guo, H.; Hu, Y.; Liu, F.; Zhong, D.; Xiong, H. Unidirectional invisibility induced by complex anti-parity–time symmetric periodic lattices. *Appl. Sci.* **2019**, *9*, 3808. [CrossRef]
21. Ke, S.; Zhao, D.; Liu, J.; Liu, Q.; Liao, Q.; Wang, B.; Lu, P. Topological bound modes in anti-PT-symmetric optical waveguide arrays. *Opt. Express* **2019**, *27*, 13858–13870. [CrossRef] [PubMed]
22. Li, H.; Xu, S.L.; Belić, M.R.; Cheng, J.X. Three-dimensional solitons in Bose-Einstein condensates with spin-orbit coupling and Bessel optical lattices. *Phys. Rev. A* **2018**, *98*, 033827. [CrossRef]
23. Xu, S.L.; Zhao, G.P.; Belić, M.R.; He, J.R.; Xue, L. Light bullets in coupled nonlinear Schrödinger equations with variable coefficients and a trapping potential. *Opt. Express* **2017**, *25*, 9094–9104. [CrossRef] [PubMed]
24. Zhao, D.; Xu, B.; Guo, H.; Xu, W.; Zhong, D. Low threshold optical bistability in aperiodic PT-symmetric lattices composited with Fibonacci sequence dielectrics and graphene. *Appl. Sci.* **2019**, *9*, 5125. [CrossRef]
25. Xu, C.; Zhang, P.; Zhao, D.; Guo, H.; Huang, M.; Ke, S. Plasmonic Jackiw-Rebbi modes in graphene waveguide arrays. *Appl. Sci.* **2019**, *9*, 4152. [CrossRef]
26. Xu, F.; Wang, J.; Zhu, X.; Liu, X. Thermodynamic modeling and experimental verification of a $NaNO_3$–KNO_3–$LiNO_3$–Ca $(NO_3)_2$ system for solar thermal energy storage. *New J. Chem.* **2017**, *41*, 10376–10382. [CrossRef]
27. Hu, Y.; Shu, T.; Mao, C.; Xue, L.; Yan, Z.; Wu, Y. Arsenene and antimonene doped by group-VA atoms: First-principles studies of the geometric structures, electronic properties and STM images. *Physica B* **2019**, *553*, 195–201. [CrossRef]
28. Xu, S.L.; Xue, L.; Belić, M.R.; He, J.R. Spatiotemporal soliton clusters in strongly nonlocal media with variable potential coefficients. *Nonlinear Dyn.* **2017**, *87*, 827–834. [CrossRef]
29. Chen, S.; Guo, Q.; Xu, S.; Belic, M.R.; Zhao, Y.; Zhao, D.; He, J. Vortex solitons in Bose-Einstein condensates with spin-orbit coupling and gaussian optical lattices. *Appl. Math. Lett.* **2019**, *92*, 15–21. [CrossRef]
30. Wang, Z.; Wang, B.; Long, H.; Wang, K.; Lu, P. Surface plasmonic lattice solitons in semi-infinite graphene sheet arrays. *J. Lightwave Technol.* **2017**, *35*, 2960–2965. [CrossRef]
31. Cheng, J.X.; Xu, S.L.; Belić, M.R.; Li, H.; Zhao, Y.; Deng, W.W.; Sun, Y.Z. Multipole solitons in a cold atomic gas with a parity-time symmetric potential. *Nonlinear Dyn.* **2019**, *95*, 2325–2332. [CrossRef]
32. Liang, H.; Xu, S.L.; Deng, W.W.; Dai, Y.; Li, H.; Belić, M.R.; Zhao, Y.; Ai, Y. Solitons in the two-dimensional fractional Schrödinger equation with radially symmetric PT potential. *Optik* **2020**, *202*, 163652. [CrossRef]
33. Deng, W.W.; Chen, S.F.; Guo, Y.W.; Li, H.; Xu, S.L.; Guo, Q.; Belić, M.J.; Zhao, Y. Two-dimensional vector solitons in a cold atomic gas via electromagnetically induced transparency. *Phys. Lett. A* **2019**, *383*, 3025–3029. [CrossRef]
34. Meng, P.; Zhao, D.; Zhong, D.; Liu, W. Topological plasmonic modes in graphene-coated nanowire arrays. *Opt. Quantum Electron.* **2019**, *51*, 156. [CrossRef]
35. Barik, S.; Miyake, H.; DeGottardi, W.; Waks, E.; Hafezi, M. Two-dimensionally confined topological edge states in photonic crystals. *New J. Phys.* **2016**, *18*, 113013. [CrossRef]
36. Ke, S.; Liu, J.; Liu, Q.; Zhao, D.; Liu, W. Strong absorption near exceptional points in plasmonic wave guide arrays. *Opt. Quantum Electron.* **2018**, *50*, 318. [CrossRef]
37. Artoni, M.; La Rocca, G.; Bassani, F. Resonantly absorbing one-dimensional photonic crystals. *Phys. Rev. E* **2005**, *72*, 046604. [CrossRef]
38. Bai, F.; Hu, Y.; Hu, Y.; Qiu, T.; Miao, X.; Zhang, S. Lead-free, air-stable ultrathin $Cs_3Bi_2I_9$ perovskite nanosheets for solar cells. *Sol. Energy Mater. Sol. Cells* **2018**, *184*, 15–21. [CrossRef]
39. Zhang, S.; Hu, Y.; Hu, Z.; Cai, B.; Zeng, H. Hydrogenated arsenenes as planar magnet and Dirac material. *Appl. Phys. Lett.* **2015**, *107*, 022102. [CrossRef]

40. Zhao, D.; Wang, Z.Q.; Long, H.; Wang, K.; Wang, B.; Lu, P.X. Optical bistability in defective photonic multilayers doped by graphene. *Opt. Quantum Electron.* **2017**, *49*, 163. [CrossRef]
41. Zhao, D.; Ke, S.; Hu, Y.; Wang, B.; Lu, P. Optical bistability in parity-time-symmetric dielectric multilayers incorporated with graphene. *J. Opt. Soc. Am. B* **2019**, *36*, 1731–1737. [CrossRef]
42. Felbacq, D.; Moreau, A.; Smaâli, R. Goos-Hänchen effect in the gaps of photonic crystals. *Opt. Lett.* **2003**, *28*, 1633–1635. [CrossRef] [PubMed]
43. Zhao, D.; Zhong, D.; Hu, Y.; Ke, S.; Liu, W. Imaginary modulation inducing giant spatial Goos-Hänchen shifts in one-dimensional defective photonic lattices. *Opt. Quantum Electron.* **2019**, *51*, 113. [CrossRef]
44. Zhao, D.; Liu, W.W.; Ke, S.L.; Liu, Q.J. Large lateral shift in complex dielectric multilayers with nearly parity–time symmetry. *Opt. Quantum Electron.* **2018**, *50*, 323. [CrossRef]
45. Zhao, D.; Liu, F.; Meng, P.; Wen, J.; Xu, S.; Li, Z.; Zhong, D. Reflection enhancement and giant lateral shift in defective photonic crystals with graphene. *Appl. Sci.* **2019**, *9*, 2141. [CrossRef]
46. Ma, P.; Gao, L. Large and tunable lateral shifts in one-dimensional PT-symmetric layered structures. *Opt. Express* **2017**, *25*, 9676. [CrossRef]
47. Rüter, C.E.; Makris, K.G.; El-Ganainy, R.; Christodoulides, D.N.; Segev, M.; Kip, D. Observation of parity–time symmetry in optics. *Nat. Phys.* **2010**, *6*, 192–195. [CrossRef]
48. Feng, L.; Xu, Y.L.; Fegadolli, W.S.; Lu, M.; Oliveira, J.E.B.; Almeida, V.R.; Chen, Y.; Scherer, A. Experimental demonstration of a unidirectional refectionless parity-time metamaterial at optical frequencies. *Nat. Mater.* **2013**, *12*, 108–113. [CrossRef]
49. Regensburger, A.; Bersch, C.; Miri, M.A.; Onishchukov, G.; Christodoulides, D.N.; Peschel, U. Parity-time synthetic photonic lattices. *Nature* **2012**, *488*, 167–171. [CrossRef]
50. Yariv, A.; Yeh, P. *Photonics: Optical Electronics in Modern Communications*, 6th ed.; Oxford University Press: New York, NY, USA, 2007.
51. Longhi, S.; Della Valle, G.; Staliunas, K. Goos-Hänchen shift in complex crystals. *Phys. Rev. A* **2011**, *84*, 042119. [CrossRef]
52. Zhu, X.F. Defect states and exceptional point splitting in the band gaps of one-dimensional parity-time lattices. *Opt. Express* **2015**, *23*, 22274–22284. [CrossRef]
53. Monfared, Y.E.; Liang, C.; Khosravi, R.; Kacerovská, B.; Yang, S. Selectively toluene-filled photonic crystal fiber Sagnac interferometer with high sensitivity for temperature sensing applications. *Results Phys.* **2019**, *13*, 102297. [CrossRef]
54. Monfared, Y.E.; Hajati, M.; Liang, C.; Yang, S.; Qasymeh, M. Quasi-d-shaped fiber optic plasmonic biosensor for high-index analyte detection. *IEEE Sens. J.* **2019**. [CrossRef]
55. Bliokh, K.Y.; Bliokh, Y.P. Conservation of angular momentum, transverse shift, and spin Hall effect in reflection and refraction of an electromagnetic wave packet. *Phys. Rev. Lett.* **2006**, *96*, 073903. [CrossRef] [PubMed]